JOURNAL OF COMPUTATIONAL PHYSICS 52, 351–373 (1983)

Regularization of Contour Dynamical Algorithms. I. Tangential Regularization

NORMAN J. ZABUSKY AND EDWARD A. OVERMAN II

Institute for Computational Mathematics and Applications, Department of Mathematics and Statistics, University of Pittsburgh, Pittsburgh, Pennsylvania 15261

Received March 30, 1981; revised April 26, 1983

Contour dynamical methods are being applied to a variety of inviscid incompressible flows in two dimensions. These generalizations of the "waterbag" method provide simplified models for following the evolution of contours $\mathbf{x}^{(j)}$ that separate regions of constant density which are the sources of the flow. The inviscid evolution of contour j, $\hat{\mathbf{x}}_t^{(j)}$ is usually an area-preserving map. For physically unstable problems, a piecewise-constant initial condition may result in an ill-posed problem. That is, contours may rapidly grow in perimeter and/or develop singularities and numerically induced small-scale structures in a finite time. To avoid such problems and model realistic weakly dissipative or weakly dispersive flows, contour regularization procedures are required. Dissipative and dispersive tangential regularization procedures for *one* contour are introduced. A special case of the former, namely $\dot{\mathbf{x}}_t = \mu \mathbf{x}_{ss}$, corresponds in lowest order to a linear diffusion operator in two dimensions. The contour is parameterized with arc length using cubic splines and an *adaptive* curvature controlled node adjustment algorithm is used. A modified Crank–Nicolson method is used to solve the discrete representation of the full system, $\mathbf{x}_t = \hat{\mathbf{x}}_t + \mu \mathbf{x}_{ss}$. Numerical results are given for the evolution of initially elliptical shapes according to prescribed area-preserving maps. The numerical results for area evolution agree with analytical results.

1. INTRODUCTION

1.1. *Survey of Developments*

Recently, there has been a renewed interest in computational studies of the evolution of ideal of nondissipative flows in two dimensions. Longuet–Higgins and Cokelet [1, 2] have studied incompressible shallow and deep water waves on boundaries between regions where density is piecewise-constant. Baker *et al.* have also considered this problem [3] as well as the Rayleigh–Taylor problem of a heavier fluid above a lighter fluid [4]. Zabusky and his associates [5–8] have investigated the Euler equations with piecewise-constant vorticity distributions. Finally, Overman and co-workers [9, 10] have been studying the evolution of weakly ionized and strongly magnetized ionospheric plasma clouds in an electric field with a piecewise-constant ion density model.

In all these cases, one is dealing with the evolution of curves in two space dimensions that separate regions of constant density. Because the densities are

0021-9991/83 $3.00

discontinuous, there are no existence theorems for many of these flows and we have no assurance that initially smooth contours remain smooth for all times. For example, we have found contours with *corners* that are steady solutions of the Euler equations with piecewise-constant vorticity [11]. Furthermore, we have computational evidence that the ionospheric plasma problem is ill-posed. That is, contours rapidly develop regions of small-scale oscillatory numerical structure. This structure appears sooner if the resolution is increased, a classical manifestation of the numerical resolution of singularities. The goal of the present study is to introduce a rational and robust tangential regularization (or smoothing) procedure that represents aspects of true dissipative or dispersive processes on each contour. These processes can inhibit the development of singularities on contours. Thus, we shall be able to calculate approximate solutions beyond small times.

Regularization, smoothing, or "cutoff" methods are well known in science and engineering. They are often introduced in an ad-hoc way when a discipline is evolving rapidly. They are needed because some asymptotic approximation to a realistic (i.e., well-posed) problem omits terms or parameters from the equations of motion or restructures the initial conditions in order to render the problem analytically or computationally tractable. The omission or restructuring may lead to ill-posed or unstable evolutionary problems. For example, Longuet-Higgins and Cokelet [1] observed a high wave-number instability arise as their smooth wave propagated. They removed this structure with a five-point smoothing (or filtering) procedure that was used every few time steps. Baker *et al.* [3] claim to have found a "dipole" procedure that delays the onset of the instabiltiy. Thus, regularization procedures are models of realistic systems, and thereby enlarge the parameter space in which approximate solutions are obtained. We shall show how *tangential* dissipative regularization embodies one essential feature of two-dimensional diffusion, namely, the decay of small-wavelength contour perturbations.

1.2. *Regularization Concepts for One- and Two-Dimensional Flows*

A cogent example of regularization is provided by Burgers' equation

$$u_t + uu_x = vu_{xx}, \qquad u(x, 0) = u_0(x), \qquad -\infty < x < +\infty, \tag{1.1}$$

an ideal model of one-dimensional pressureless hydrodynamics, where $v > 0$ is a constant viscous parameter. For bounded and smooth $u_0(x)$, (1.1) has unique solutions and bounded derivatives for all times [12, 13]. However, if one "simplifies" the problem by setting $v = 0$, the resulting Euler equation has the general solution

$$u(x, t) = u_0(x - u(x, t)\, t),$$

and derivatives of u become singular at a time $t_B = |\min u_0'|^{-1}$. Thus, for $v > 0$, characteristics are "prevented" from crossing.

Similarly, for computational studies of shock-wave problems in one dimension with

negligibly small "true" viscosity, Richtmyer and von Neumann [14, 15] advocated the addition of a small-but-finite artificial or pseudononlinear viscosity to regularize the problem. In essence, they replaced the pressure p by $p + q$, where

$$\begin{aligned} q &= (\bar{\nu}\tau)(u_x)^2 \qquad \text{if} \quad u_x < 0, \\ &= 0 \qquad\qquad\ \ \text{if} \quad u_x \geqslant 0, \end{aligned} \tag{1.2}$$

has units of $(L/T)^2$ and $\bar{\nu}\tau$ is proportional to the fluid density ρ/ρ_0. They applied this regularization procedure to numerical solutions of one-dimensional compressible gas dynamics and verified that, for small shock thickness, the variation in dependent variables across the transition layer agrees with the jump relations obtained from Hugoniot theory. In recent years, linear higher-order dissipative processes [15] have been used in fluid dynamical simulations in one and two dimensions, e.g., $q = (\bar{\nu}l^2 u_{xxx})$ replaces (νu_x).

For two-dimensional nearly inviscid incompressible fluids the problem is more complicated. There are no steady-state solutions, corresponding to the Hugoniot relations, with which to make validating comparisons. For example, the vorticity-stream function form of the incompressible Navier–Stokes equations

$$\omega_t + \psi_y \omega_x - \psi_x \omega_y = \nu \Delta\omega, \qquad \Delta\psi = -\omega \tag{1.3}$$

(where $\omega(x, y, 0) = \omega_0(x, y)$) have been used to study 2D fluid turbulence [17, 18].

For the Euler equations, obtained with $\nu = 0$, all isovorticity contours are convected with the flow (Helmholtz's theorem). Zabusky *et al.* [5 – 8] have further idealized the inviscid problem by assuming ω_0 is a piecewise-constant function. Hence, ω remains piecewise-constant and the problem is reduced to the self-consistent interaction of contours that separate regions of constant ω. If $\omega_0(x, y)$ is Hölder continuous and in a bounded domain, then ω remains Hölder continuous and velocity gradients are bounded for all times [17].

If ν is finite we know that (1) if ω_0 is piecewise-constant or smoother, regular solution exist for any finite time [17]; (2) the integrals of ω^n (n even) of isolated vortex distributions of one sign decrease monotonically in time; and (3) topology changes may occur, that is, isovorticity lines may reconnect.

For example, topology changes may occur after the shear (Kelvin–Helmholtz) instability has greatly disturbed a weakly perturbed set of isovorticity lines. See frame a ($t = 0$) of Fig. 1 (which is Fig. 8 of Zabusky and Deem [19]) which shows isovorticity contours (positive contours are solid and negative are dashed of a simulation with $\mathrm{Re} = 750$ on a 128^2 grid with the flow confined near the center. As the process evolves, the isovorticity lines elongate and approach each other in certain regions. The strong vorticity gradients increase dissipation locally which manifests itself in contour pinching and rapid disappearance of long sharp (high-curvature) filaments. (see (†) in frames b and e.) In frame f we are left with several isolated rounded regions of vorticity. The region marked "secondary" in frame f arises from the

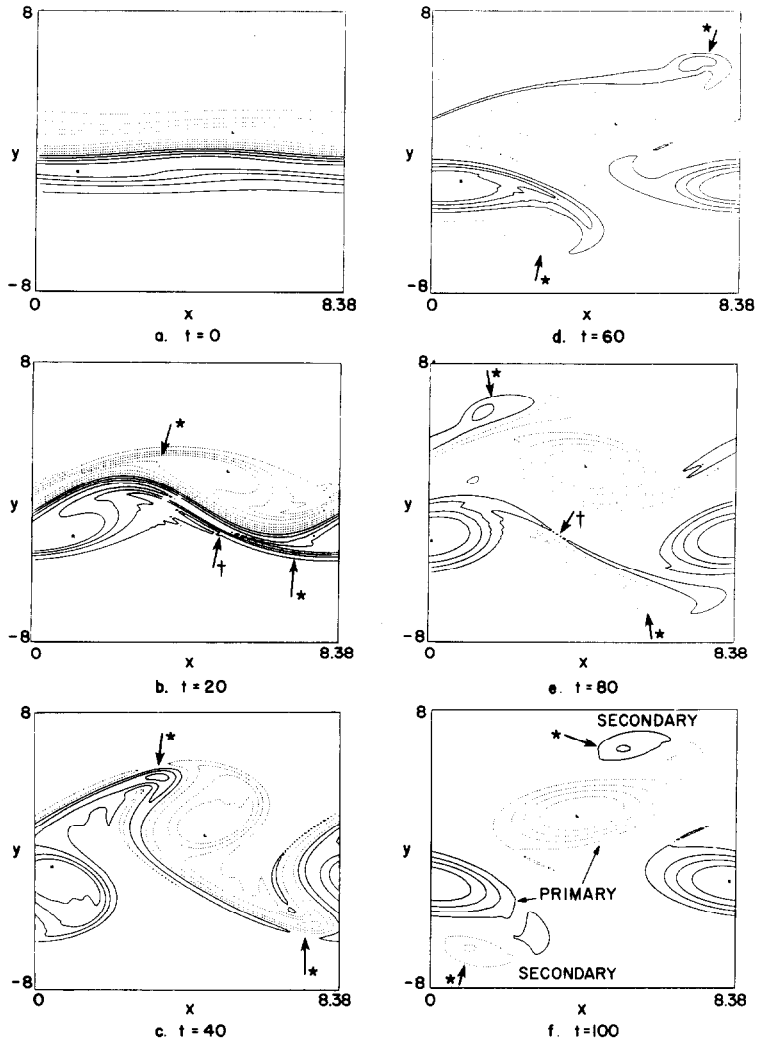

FIG. 1. Evolution of constant vorticity contours (9 levels) for a perturbed Gaussian profile that models a wake. (This is an augmented version of Fig. 8 in Ref. [19].)

entrainment of *opposite*-signed vorticity, which we follow in the figure with the asterisked arrows.

In Section 2.1 we derive higher-order dissipative and dispersive regularization procedures which inhibit the formation of contour singularities. The simplest dissipative algorithm includes terms in the evolution equations containing second partial derivatives with respect to arc length (proportional to local curvature). This causes the area and perimeter to decrease, the latter mainly in sharp regions of large curvature. In Section 2.2 we show how this procedure corresponds, in lowest order,

with the solution of the two-dimensional problem $\omega_t = \nu \Delta\omega$ for special initial conditions. In Section 3.1 we describe algorithms for discretizing the continuum representation of Section 2. In Section 3.2 we include a robust curvature controlled adaptive algorithm for node-insertion-and-removal which maintains the product of (density-of-nodes) times (local curvature) to within a narrow range. In essence, the contour is parameterized by discrete nodes whose density as a function of arc length varies (adapts) inversely proportional to the local curvature. In Section 4 we present numerical results. In the concluding section we discuss concepts for multicontour regularization, a procedure necessary to obtain solutions at intermediate times. We shall consider, at another time, the contour reconnection problem associated with merging regions and pinching filaments.

2. Continuum Theory of Regularization

2.1. *Tangential Regularization*

The contours evolving in the plane are parameterized by σ and t. We parameterize contours both by the location of nodes in the plane

$$\mathbf{x} \equiv (x(t, \sigma), y(t, \sigma)), \tag{2.1}$$

and by arc length derivative and local tangent angle $(g(t, \sigma), \phi(t, \sigma))$, where

$$g \equiv s_\sigma = [x_\sigma^2 + y_\sigma^2]^{1/2}. \tag{2.2}$$

In the latter case, we also require the location of a point on the contour.

If we take the time derivative of (2.2) we obtain

$$g_t = x_{\sigma t} \cos\phi + y_{\sigma t} \sin\phi, \tag{2.3}$$

where

$$\cos\phi = x_\sigma / g \equiv x_s, \qquad \sin\phi = y_\sigma / g \equiv y_s. \tag{2.4}$$

If we differentiate $\tan\phi = y/x$ with respect to time and simplify, we obtain

$$g\phi_t = -x_{\sigma t} \sin\phi + y_{\sigma t} \cos\phi. \tag{2.5}$$

Thus, there is a unitary transformation between the two representations $(x_\sigma, y_\sigma)_t \leftrightarrows (g_t, g\phi_t)$, where

$$(x_\sigma, y_\sigma)_t = (g_t, g\phi_t)\, U \equiv (g_t, g\phi_t) \begin{pmatrix} \cos\phi & \sin\phi \\ -\sin\phi & \cos\phi \end{pmatrix}. \tag{2.6}$$

The curvature κ is given by

$$\kappa \equiv \phi_s = \phi_\sigma / s_\sigma = (x_\sigma y_{\sigma\sigma} - y_\sigma x_{\sigma\sigma}) / (x_\sigma^2 + y_\sigma^2)^{3/2}, \tag{2.7}$$

where

$$\int \kappa \, ds = \int_0^{2\pi} d\phi = 2\pi. \tag{2.8}$$

Assume that the evolution equations can be written as a sum of two terms

$$(g, \phi)_t = (\hat{g}, \hat{\phi})_t + (G, \Phi), \tag{2.9}$$

or

$$(x, y)_t = (\hat{x}, \hat{y})_t + (X, Y), \tag{2.10}$$

where $(\hat{g}, \hat{\phi})_t$ or $(\hat{x}, \hat{y})_t$ represent convective, usually area-preserving, terms and (G, Φ) or (X, Y) are the dissipative and/or dispersive regularization terms we are seeking. For example, for the Euler equations, $(\hat{x}, \hat{y})_t$ is obtained from by integrating around contours ∂D_j that separate piecewise-constant regions of vorticity [5], or

$$\hat{\mathbf{x}}_t \equiv (\hat{x}, \hat{y})_t = (2\pi)^{-1} \sum_j [\omega]_j \int_{\partial D_j} \log r(d\xi, d\eta),$$

where $r^2 = (x-\xi)^2 + (y-\eta)^2$ and $[\omega]_j = \omega_{j,\text{outside}} - \omega_{j,\text{inside}}$.

We now differentiate (2.10) with respect to σ and substitute (2.6) to obtain

$$(X_\sigma, Y_\sigma) = (G, g\Phi)\, U. \tag{2.11}$$

We now require that the right side of (2.11) be perfect derivatives of σ. Hence, if

$$X = \mathscr{F} \cos\phi - \mathscr{G} \sin\phi \qquad \text{and} \qquad Y = \mathscr{F} \sin\phi + \mathscr{G} \cos\phi, \tag{2.12}$$

then for consistency

$$G = \mathscr{F}_\sigma - \phi_\sigma \mathscr{G}, \tag{2.13a}$$

and

$$g\Phi = \mathscr{G}_\sigma + \mathscr{F}\phi_\sigma. \tag{2.13b}$$

We simplify possibilities by setting $\mathscr{F} \equiv 0$ and find

$$G = -\phi_\sigma \mathscr{G} \tag{2.14a}$$

and

$$\Phi = \mathscr{G}_s. \tag{2.14b}$$

The contour evolution equations become

$$(g, \phi)_t = (\hat{g}, \hat{\phi})_t + (-g\kappa\mathscr{G}, \mathscr{G}_s) \tag{2.15}$$

or

$$(x, y)_t = (\hat{x}, \hat{y})_t + \mathscr{G}(-\sin\phi, \cos\phi). \tag{2.16}$$

For processes which are dissipative (i.e., where contours become rounded, shrink, and vanish in time) we take $\mathscr{G} = \mathscr{G}_1$, where

$$\mathscr{G}_1 = \mu_1 |\kappa|^{p-1} \kappa. \tag{2.17}$$

For processes which are dispersive (such as surface tension where interfaces persist and oscillate in time) we take $\mathscr{G} = \mathscr{G}_2$, where

$$\mathscr{G}_2 = \mu_2 \partial_s (|\kappa|^{q-1} \kappa). \tag{2.18}$$

If p and q are >1, we have nonlinear coefficients of dissipative and dispersive regularization in (2.17) and (2.18), respectively. The former is analogous to the nonlinear viscosity introduced by von Neumann and Richtmyer [14]. For example, if $\mu_2 = 0$ and $p = 1$, we obtain

$$\phi_t = \hat{\phi}_t + \mu_1 \phi_{ss} \qquad \text{and} \qquad g_t = \hat{g}_t - \mu_1 g\kappa^2, \tag{2.19}$$

or

$$(x, y)_t = (\hat{x}, \hat{y})_t + \mu_1 (x_{ss}, y_{ss}). \tag{2.20}$$

The last follows because

$$-\kappa \sin\phi \equiv -\phi_s \sin\phi = (\cos\phi)_s = x_{ss},$$

and similarly $\kappa \cos\phi = y_{ss}$. These equations are intrinsically nonlinear, for they are coupled through arc-length derivatives, e.g., $\partial_s \equiv g^{-1} \partial_\sigma$. Equation (2.20) with $(\hat{x}, \hat{y})_t \equiv 0$ has been described by Brakke as the evolution of a curve by its "mean curvature," a concept which is generalizable to the evolution of surfaces in higher dimensions [20].

An alternate and concise view of these motions is obtained by examining the evolution of curvature,

$$\begin{aligned} &\kappa_t \equiv (\phi_\sigma / g)_t = g^{-1} (\phi_\sigma)_t - g^{-1} g_t \kappa, \\ \text{or} \quad &\kappa_t = ((\hat{\phi}_t)_s - \kappa g^{-1} \hat{g}_t) + (\mathscr{G}_{ss} + \kappa^2 \mathscr{G}), \end{aligned} \tag{2.21}$$

where $\hat{\phi}_t$ and $\hat{g}_t$ are defined in (2.9). For dissipative regularization ($p = 1$)

$$\kappa_t = \mu_1 (\kappa^3 + \kappa_{ss}) \qquad \text{and} \qquad (\ln g)_t = -\mu_1 \kappa^2 \tag{2.22}$$

and for dispersive regularization ($q = 1$)

$$\kappa_t = \mu_2 (\kappa^2 \kappa_s + \kappa_{sss}) \qquad \text{and} \qquad (\ln g)_t = -(\mu_2 / 2)(\kappa^2)_s. \tag{2.23}$$

Equation (2.23) is the modified Korteweg–de Vries equation which supports *soliton* solutions [21]. The leading term in (2.22) may seem paradoxical, but it follows from the decrease in perimeter (or radius) due to regularization. That is, if we start with a circle, then $\kappa_{ss} = 0$ and

$$\kappa^{-2} = \kappa_0^{-2} - 2\mu_1 t \qquad \text{or} \qquad r^2 = r_0^2 - 2\mu_1 t. \tag{2.24}$$

The last relation is not unexpected, for it arises in the argument of the Green's function for two-dimensional linear parabolic equations.

We now examine the evolution of the perimeter $P = \oint ds$ and the area $A = -\oint y\, dx = -\oint y x_\sigma\, d\sigma$. The rate of change of perimeter

$$P_t = \oint g_t\, d\sigma = \hat{P}_t - \oint \kappa \mathscr{G}\, ds = \hat{P}_t - \mu_1 \oint |\kappa|^{p+1}\, ds - \mu_2 \oint \kappa(\partial_s |\kappa|^{q-1}\kappa)\, ds, \tag{2.25}$$

where the dispersive term vanishes identically, when q is odd and >0. Thus, with dissipative regularization, regions of large curvature cause the main decrease in perimeter. The time rate-of-change of area is

$$A_t = -\int (y_t x_\sigma + y x_{\sigma t})\, d\sigma = \int (-y_t x_\sigma + x_t y_\sigma)\, d\sigma, \tag{2.26a}$$

$$= \hat{A}_t - \oint \mathscr{G}\, ds = \hat{A}_t - \mu_1 \int_0^{2\pi} |\kappa|^{p-1}\, d\phi, \tag{2.26b}$$

where $\hat{A}_t$ results from the convective part of the map and (2.26b) results after substituting $\mathscr{G} = \mathscr{G}_1 + \mathscr{G}_2$. Note that dispersive regularization does not affect area invariance. Note also for $p = 1$ and $\hat{A}_t = 0$

$$P_t = \hat{P}_t - \mu_1 \oint \kappa^2\, ds \tag{2.27a}$$

and

$$A_t = -2\pi\mu_1, \tag{2.27b}$$

where (2.27b) is consistent with (2.24). Brakke also shows that the total curvature, $\oint_{\partial D} |\kappa|\, ds$, is monotone decreasing for each $t \in [0, t_1]$ [20, Appendix B, Proposition 2]. If $p > 1$ the perimeter and area will decrease more rapidly.

2.2. *Tangential Regularization and 2D Diffusion*

For initial value problems the 2D diffusion equation

$$\omega_t = \nu \Delta\omega \tag{2.28}$$

acts to decrease (or spread) steep gradients and to smooth small-scale oscillatory perturbations of an initial state. Obviously a one-contour model cannot deal with the first phenomenon. We discuss multicontour representations in Sections 5. We now

clarify the correspondence between (2.28) and dissipative tangential regularization ($\mathscr{F}=0$ and $\mathscr{G}=\mu\kappa$) by examining the evolution two piecewise-constant initial conditions. First we consider

$$\Gamma(t=0)=\{(x,y)\,|\,y=\varepsilon\cos mx\},\qquad 0<\varepsilon\ll 1,\quad m=O(\varepsilon^{-1/2}) \tag{2.29}$$

for contour dynamics and

$$\begin{aligned}\omega(x,y,0)&=1 \qquad \text{if}\quad y<\varepsilon\cos mx,\\ &=0 \qquad \text{if}\quad y>\varepsilon\cos mx,\end{aligned} \tag{2.30}$$

for (2.28). In Appendix A we show that (2.29) becomes

$$\Gamma(t)=\{(x,y)\,|\,y=\varepsilon e^{-\mu m^2 t}\cos mx+O(\varepsilon^{3/2})\}. \tag{2.31}$$

When (2.30) evolves ω does not remain piecewise-constant, but it is very steep for a time. To compare (2.31) with the solution of (2.28) and (2.30), we examine the line $\tilde{y}(x,t)$ defined by

$$\omega(x,\tilde{y},t)=\tfrac{1}{2}\Omega \tag{2.32}$$

and obtain

$$\tilde{y}(x,t)=\varepsilon e^{-\nu m^2 t}\cos mx+O(\varepsilon^{3/2}), \tag{2.33}$$

as shown in Appendix A.

For our second example we consider the analogous perturbed-circle initial conditions

$$\Gamma(t=0)=\{(r,\theta)\,|\,r=r_0+\varepsilon\cos m\theta\},\qquad 0<\varepsilon\ll 1\quad m=O(\varepsilon^{-1/2}) \tag{2.34}$$

for contour dynamics, and

$$\begin{aligned}\omega(r,\theta,t=0)&=1 \qquad \text{if}\quad r<r_0+\varepsilon\cos m\theta,\\ &=0 \qquad \text{if}\quad r>r_0+\varepsilon\cos m\theta,\end{aligned} \tag{2.35}$$

for (2.28). Similarly, one can show that

$$\Gamma(t)=\{(r,\theta)\,|\,r=r_0-\mu t/r_0+\varepsilon e^{-\mu m^2 t/r_0^2}\cos m\theta+O(\varepsilon^{3/2})\} \tag{2.36}$$

for contour dynamics and

$$\tilde{r}(\theta,t)=r_0-\nu t/r_0+\varepsilon e^{-\nu m^2 t/r_0^2}\cos m\theta+O(\varepsilon^{3/2}), \tag{2.37}$$

for (2.24), where $\tilde{r}(\theta,t)$ is the line defined by

$$\omega(\tilde{r},\theta,t)=\tfrac{1}{2}\Omega. \tag{2.38}$$

Thus, if $\mu = \nu$ both forms agree to lowest order for the evolution of small-wavelength terms. These results elucidate (2.27a). That is, large-κ fluctuations contribute to a rapid decrease in perimeter. The contour contraction in (2.37) is not surprising, because the maximum of $\omega(x, y, t)$ is decaying and eventually all finite height contours of ω vanish.

3. Discretization and Evolution of Regularized Contours

3.1. *Discretization of Tangential Dissipative Regularization*

We first discuss procedures for approximating a contour by periodic cubic splines (PCS), as shown in Fig. 2. Details are given in Appendix B. This procedure includes a node-adjustment algorithm which is discussed in the next section. The time advancement of each node is done with an implicit predictor and an implicit corrector which both require the inversion of periodic tridiagonal matrices. For convenience we let $\hat{\mathbf{x}}_t \equiv \dot{\hat{\mathbf{x}}}$ in this section.

At any time, the contour is represented by the set of nodes $\{(x_j, y_j) \mid 1 \leqslant j \leqslant N\}$, where $(x_{N+1}, y_{N+1}) = (x_1, y_1)$. The complete contour is determined in two steps, as described in detail in Appendix B. First, we obtain a contour $\tilde{\Gamma}$ which passes through all the nodes and which is parameterized by the straight-line distance between adjacent nodes, l. Thus, $\tilde{\Gamma} = \{(\tilde{x}(l), \tilde{y}(l))\}$, where $\tilde{x}$ and $\tilde{y}$ are periodic cubic splines.

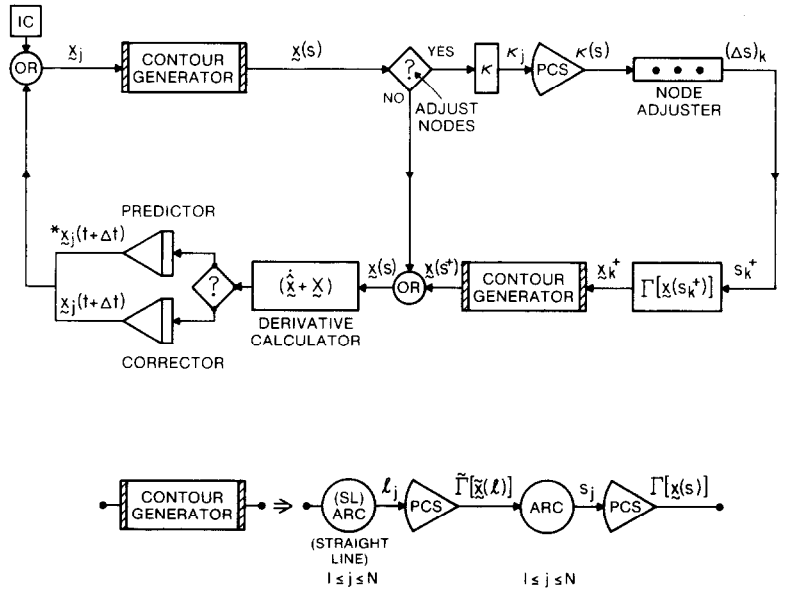

FIG. 2. Flowchart for contour calculation including node adjustment. Note, here and in Section 3, that $\dot{\hat{\mathbf{x}}} \equiv \hat{\mathbf{x}}_t$.

Next, we calculate the arc length between adjacent nodes on $\tilde{\Gamma}$ using an adaptive quadrature rule which yields results with a prescribed accuracy and obtain the desired contour $\Gamma = \{(x(s), y(s))\}$.

If we define the central-difference operator

$$\delta x_j = x(s_{j+1/2}) - x(s_{j-1/2}),$$

with a similar expression for δy_j and $\delta s_j = s_{j+1/2} - s_{j+1/2}$, then the second derivative x_{ss} is discretized as

$$D_j(x, s) = 2(s_{j+1} - s_{j-1})^{-1}[(\delta x_{j+1/2}/\delta s_{j+1/2}) - (\delta x_{j-1/2}/\delta s_{j-1/2})]. \tag{3.1}$$

In the continuum limit (3.1) becomes

$$D_j(x, s) = x_{ss} + \tfrac{1}{3}[\delta s_{j+1/2} - \delta s_{j-1/2}]\, x_{sss} + \tfrac{1}{12}[(\delta s_{j+1/2})^2 - (\delta s_{j+1/2})(\delta s_{j-1/2}) + (\delta s_{j-1/2})^2]\, x_{ssss} + O((\delta s)^2), \tag{3.2}$$

and we observe that the algorithm is first order if $\delta s_{j-1/2} \neq \delta s_{j+1/2}$. A similar result holds for y_{ss}.

We advance (2.20) with a predictor and one (or more) correctors. That is, for x in (2.20) we obtain the predicted ${}^*x_j^{n+1}$ from

$$({}^*x_j^{n+1} - x_j^n)/\Delta t = \hat{x}_j^n + \mu D_j({}^*x^{n+1/2}, s^n), \tag{3.3}$$

where the superscript n designates the time level, and define

$${}^*x_j^{n+1/2} \equiv \tfrac{1}{2}({}^*x_j^{n+1} + x_j^n), \tag{3.4}$$

where $\hat{\mathbf{x}}_j^n$ is the contribution resulting from discretizing $\hat{\mathbf{x}} \equiv \hat{\mathbf{x}}_t$. Equation (3.3) with (3.4) is a generalization of the Crank–Nicolson method. Since D_j is linear in ${}^*x_j^{n+1}$ we can combine it with the left side and obtain a periodic tridiagonal matrix in ${}^*x_j^{n+1}$. To obtain a higher-order scheme, one could replace (3.1) with differences based on five adjacent nodes and one would have to invert a periodic five-diagonal matrix. Similarly,

$$({}^*y_j^{n+1} - y_j^n)/\Delta t = \hat{y}_j^n + \mu D_j({}^*y^{n+1/2}, s^n). \tag{3.5}$$

The corrector formula is

$$(x_j^{n+1} - x_j^n)/\Delta t = {}^*\hat{x}_j^{n+1/2} + \mu D_j(x^{n+1/2}, {}^*s^{n+1/2}), \tag{3.6}$$

where

$$\begin{aligned} {}^*\hat{x}_j^{n+1/2} &\equiv \tfrac{1}{2}({}^*\hat{x}_j^{n+1} + \hat{x}_j^n), \\ x_j^{n+1/2} &\equiv \tfrac{1}{2}(x_j^{n+1} + x_j^n), \end{aligned} \tag{3.7}$$

and

$${}^*s_j^{n+1/2} \equiv \tfrac{1}{2}({}^*s_j^{n+1} + s_j^n).$$

That is, the arc length ${}^*s_j^{n+1}$ and the convective time evolution ${}^*\dot{x}_j^{n+1}$ are computed using the predicted nodes $({}^*x_j^{n+1}, {}^*y_j^{n+1})$. The formulas used in the program are written in matrix form as

$$[1 + a^m](x^{n+1}) = \Delta t(\hat{\dot{x}}^m) + [1 - a^m](x^n), \tag{3.8}$$

where a^m is cyclic tridiagonal matrix with elements

$$\begin{aligned}(\alpha^m)_{j,j-1} &= -\mu\,\Delta t(\delta s^m_{j-1/2} + \delta s^m_{j+1/2})^{-1}(\delta s^m_{j-1/2})^{-1},\\ (\alpha^m)_{j,j+1} &= -\mu\,\Delta t(\delta s^m_{j-1/2} + \delta s^m_{j+1/2})^{-1}(\delta s^m_{j+1/2})^{-1},\\ (a^m)_{j,j} &= -(a^m)_{j,j-1} - (a^m)_{j,j+1},\end{aligned} \tag{3.9}$$

and where $m = n$ for the predictor and $m = n + \frac{1}{2}$ for the corrector.

3.2. *Curvature-Controlled Node Adjustment Algorithm*

For area-preserving maps the perimeter may grow indefinitely if instabilities or nonlinear filamentation processes are present. Thus, to control the growth of truncation errors and to minimize computation, we insert, remove, and adjust nodes according to the magnitude of the local curvature of Γ after an a priori prescribed number of time steps (the question mark in Fig. 2). Here we shall outline a nonunique

We represent $\Gamma = \{(x(s), y(s))\}$ by $\{(s, \kappa(s))\}$, where κ is the periodic cubic spline fit to the curvature calculated from the periodic cubic spline representation of $\{(x(s), y(s))\}$. First, we divide the curve into *segments* in which the curvature varies *monotonically*. In each segment we adjust the nodal intervals to satisfy certain constraints where we begin at the end which has the larger $|\kappa|$ and march to the other end. We attempt to set the new internodal distance, $h_k \equiv s_{k+1} - s_k$, at s_k to

$$h_k^* \equiv c_1/|\kappa(s_k)|, \tag{3.10}$$

but we require that h_k^* satisfy two constraints:

$$h_{\max} \geqslant h_k^* \geqslant h_{\min}, \tag{3.11}$$

and

$$(1 - r)\,h_{k-1} \leqslant h_k^* \leqslant (1 + r)\,h_{k-1}. \tag{3.12}$$

The upper limit $h_{\max}$ guarantees a minimal a priori accuracy, which, for example, is necessary for solving problems where the advective velocity $(\hat{\mathbf{x}})_t$ is obtained from the solution of an integral equation [9, 10]. The lower limit guarantees a maximum accuracy and also prevents the number of nodes from growing too rapidly. The value of $h_{\min}$ depends upon μ (which determines a true scale size). Equation (3.12) controls

the ratio of adjacent internodal distances. Hence, if h_k^* lies within the range $[h_{\max}, h_{\min}]$, our algorithm is

$$\begin{aligned} &h_k = h_k^* && \text{if} \quad h_k^* \lesssim (1 \pm r)\, h_{k-1}, \\ \text{or} \quad &h_k = (1 \pm r)\, h_{k-1} && \text{if} \quad h_k^* \gtrsim (1 \pm r)\, h_{k-1}. \end{aligned} \tag{3.13}$$

The parameter r is 0.3 in all the runs in this paper. (In recent studies of the Euler equations [8], we have found that if (3.10) is replaced by $h_k^* \equiv c_1/|\kappa(S_k)|^\beta$, where $0.25 < \beta < 0.4$, then more accurate results are obtained.)

The order in which the segments are adjusted depends on the maximum $|\kappa|$ in each segment. The algorithm begins with the segments with the largest maximum $|\kappa|$ and ends with the segments with the smallest. (There are always at least two segments with the same maximum $|\kappa|$.) This guarantees that the regions of large curvature (i.e., small-scale structures) are well resolved, which is the primary aim of the algorithm. However, it does not guarantee that the ratio of internodal distances will satisfy (3.12) at the boundaries between segments. Thus, some segments may have to be redone—but generally not more than 2 times. Note that the use of segments is essential in contours where narrow regions of large curvature develop, as shown in Fig. 3, because it avoids the problem of readjusting nodes in the vicinity of these narrow large-curvature regions or of "skipping-over" them. Note that the selection of parameters c_1, $h_{\max}$, and $h_{\min}$ depends both on μ and on the accuracy of the method of calculating the inviscid component of the advective velocity, $\dot{\hat{\mathbf{x}}}$.

After all segments have been adjusted, we have the locations of the desired nodes $\{s_k^+ \mid 1 \leqslant k \leqslant \tilde{N}\}$, where $\tilde{N}$ is the new number of nodes. Using the periodic cubic spline representations for Γ, we obtain the location of the new nodes $\{(x(s_k^+), y(s_k^+)) \mid 1 \leqslant k \leqslant \tilde{N}\}$.

4. Discussion of Numerical Computations

In this section we present computations which illustrate properties of dissipative tangential regularization with node adjustment. In each case we begin with an ellipse and for our advective flows $\hat{\mathbf{x}}_t$ we use three area-preserving maps:

(1) translation,

$$(\hat{x}, \hat{y})_t = (v_1, v_2); \tag{4.1a}$$

FIG. 3. Graphs of (a) 1:0.25 ellipse described in Table Ia and (b) 1:0.125 ellipse described in Table Ic at times, 0, 1, 4, both in a rotating frame of reference.

(2) rotation,

$$(\hat{x}, \hat{y})_t = \Omega_0(-y, x); \tag{4.1b}$$

and

(3) differential rotation,

$$\begin{aligned}(\hat{x}, \hat{y})_t &= \Omega_0(-y, x) \qquad \text{if} \quad 0 \leqslant r \leqslant r_0 \\ &\equiv \Omega_0(r_0/r)^2(-y, x) \qquad \text{if} \quad r > r_0,\end{aligned} \tag{4.1c}$$

where $r = (x^2 + y^2)^{1/2}$. In the above v_1, v_2, Ω_0, and r_0 are constants.

The predictor-corrector algorithm, described in Section 3.1, was used with $\Delta t = 0.01$ or 0.02 and a node adjustment was done every 0.20 units of time.

The quality of the runs is seen by comparing the number of nodes N, the area A, the perimeter P, and the maximum and minimum curvatures $\kappa_{\max}$ and $\kappa_{\min}$ (as described in Appendix B) as a function of time. The true area $A_{\text{tr}} = A(0) - 2\pi\mu t$ (see (2.27b)) is also given along with the relative error in the area, $\varepsilon_A = (A_{\text{tr}} - A_{\text{num}})/A_{\text{tr}}$. We compute the area A_{num} by applying the adaptive integration routine, described in Appendix B, to $A = -\oint y\, dx$, where the line integral is over the contour. (The relative error is 10^{-5} and the absolute error is 10^{-4}.)

The initial conditions for advections (4.1a) and (4.1b) were ellipses with major-axis: minor-axis of 1: 0.25 and 1: 0.125. Results are given, respectively, in Tables Ia and Ic for the former (where $c_1 = 0.03$, $h_{\min} = 0.001$, $h_{\max} = 0.03$, and $N(0) = 283$ and 271) and Tables Ib and Id for the latter (where $c_1 = 0.01$, $h_{\min} = 0.00025$, $h_{\max} = 0.01$, and $N(0) = 831$ and 843). The two discretizations were used to assess truncation errors. Note that the precise value of $N(0)$ was chosen by the node

TABLE Ia

The Evolution of a 1: 0.25 Rotating Ellipse with $\Omega_0 = 1.0$ (rad/sec) and $\mu = 0.002$[a]

t	N	P	A_{tr}	ε_A	$\kappa_{\max}$	$\kappa_{\min}$
0.0	283	4.2892	0.78540	0	16.01	0.2500
0.2	282	4.2717	0.78289	0	14.23	0.2503
0.4	280	4.2550	0.78037	−1.3	13.27	0.2505
0.6	280	4.2388	0.77786	−1.3	12.64	0.2508
0.8	280	4.2229	0.77535	−1.3	12.14	0.2511
1.0	280	4.2075	0.77283	−2.6	11.74	0.2514
2.0	278	4.1338	0.76027	−2.6	10.47	0.2529
3.0	276	4.0645	0.74770	−5.3	9.73	0.2545
4.0	274	3.9980	0.73514	−6.8	9.22	0.2561

[a] Single precision, $\Delta t = 0.02$; $h_{\min} = 0.001$ and $h_{\max} = 0.03$.

TABLE Ib

The Evolution of a 1: 0.25 Rotating Ellipse with $\Omega_0 = 1.0$ (rad/sec) and $\mu = 0.002$[a]

t	N	P	A_{tr}	ε_A	κ_{max}	κ_{min}
0.0	831	4.2892	0.78540	0	16.00	0.2500
0.2	831	4.2717	0.78289	0	14.21	0.2503
0.4	828	4.2550	0.78037	0	13.27	0.2506
0.6	828	4.2388	0.77786	0	12.62	0.2509
0.8	827	4.2230	0.77535	0	12.13	0.2512
1.0	826	4.2075	0.77283	0	11.74	0.2515
2.0	821	4.1338	0.76027	0	10.47	0.2530
3.0	815	4.0644	0.74770	0	9.73	0.2545
4.0	808	3.9978	0.73514	0	9.22	0.2561

[a] The resolution is increased fourfold from Table Ia. Double precision, $\Delta t = 0.01$; $h_{min} = 0.00025$ and $h_{max} = 0.01$.

TABLE Ic

The evolution of a 1: 0.125 Rotating Ellipse with $\Omega_0 = 1.0$ (rad/sec) and $\mu = 0.002$[a]

t	N	P	A_{tr}	ε_A	κ_{max}	κ_{min}
0.0	271	4.0931	0.39270	0	64.19	0.1250
0.2	297	4.0377	0.39019	−2.6	37.47	0.1251
0.4	304	3.9917	0.38767	−5.2	32.53	0.1253
0.6	306	3.9499	0.38516	−7.8	29.31	0.1254
0.8	305	3.9107	0.38265	−7.8	27.57	0.1256
1.0	303	3.8735	0.38013	−13.2	25.44	0.1257
2.0	297	3.7056	0.36757	−19.0	21.29	0.1263
3.0	292	3.5554	0.35500	−28.2	19.25	0.1273
4.0	288	3.4159	0.34243	−35.0	17.94	0.1282

[a] Single precision, $\Delta t = 0.02$; $h_{min} = 0.001$ and $h_{max} = 0.03$.

adjustment algorithm, as determined by (3.10), (3.11), and (3.13). The small-N calculations were made in single precision (8 significant figures on the University of Pittsburgh DEC-10). To avoid small amplitude-and-wavelength numerical curvature oscillations, the large-N runs were made in double precision. The effect of the higher resolution can be seen in $\kappa_{max}(0)$ which should be 16.0 and 64.0 for the 1: $(\frac{1}{4})$ or 1: $(\frac{1}{8})$ ellipses, respectively.

For uniform translation (4.1a), our algorithm was studied, without loss of generality, with $v_1 = v_2 = 0$. For uniform rotation (4.1b), we set $\Omega_0 = 1$ radian per unit time and obtained nearly identical results and so we discuss only the latter. As

TABLE Id

The evolution of a 1: 0.125 Rotating Ellipse with $\Omega_0 = 1.0$ (rad/sec) and $\mu = 0.002$[a]

t	N	P	A_{tr}	ε_A	κ_{max}	κ_{min}
0.0	843	4.0931	0.39270	0	64.05	0.1250
0.2	898	4.0376	0.39019	0	36.69	0.1251
0.4	898	3.9914	0.38767	0	31.46	0.1253
0.6	898	3.9494	0.38516	0	28.59	0.1254
0.8	894	3.9102	0.38265	0	26.67	0.1256
1.0	892	3.8730	0.38013	−2.6	25.25	0.1258
2.0	879	3.7048	0.36757	−2.7	21.25	0.1265
3.0	867	3.5545	0.35500	−2.8	19.21	0.1273
4.0	853	3.4148	0.34243	−5.8	17.91	0.1282

[a] The resolution is increased fourfold from Table Ic. Double precision, $\Delta t = 0.01$; $h_{min} = 0.00025$ and $h_{max} = 0.01$.

time evolved we observed a rapid initial decrease in curvature followed by a slower decrease. Thus, for the $1:\frac{1}{4}$ ellipse, where $\Delta t = 0.02$, the maximum curvature decreased by 26% between $0 \leqslant t \leqslant 1.0$ while it decreased by 16% in $1.0 \leqslant t \leqslant 4.0$. Also the number of points slowly decreases with time. Note that Tables Ia and Ib are nearly identical and that the effect of the higher resolution can be seen in ε_A which is, in fact, zero to 5 significant digits in Table Ib. For the $1:(\frac{1}{8})$ ellipse, where $\Delta t = 0.02$ for the low-resolution run and $\Delta t = 0.01$ for the high-resolution run, the situation is more complicated. The curvature did again decrease—by 40% in $0 \leqslant t \leqslant 1.0$ and 12% in $1.0 \leqslant t \leqslant 4.0$ but the number of nodes *increased* initially. The reason lies in the observation that although the curvature is *decreasing* in time in a very small neighborhood of the tip, there are nearby regions of smaller (but still large) curvature where the curvature is *increasing* in time initially. The competition between these processes results in an initial rapid increase in N from 843 to 898. This competition in fact, leads to the appearance of spurious maxima 0.0006 units from the tip when $\Delta t = 0.02$. We are certain that these new maxima were due to the larger time step and not the node distribution. Our evidence is that they disappeared when we set $\Delta t = 0.01$ and 0.005, but did not disappear (and were resolved very well) when we kept $\Delta t = 0.02$, increased the number of points near the tip, and turned off the node-adjustment algorithm.

The third advective flow (4.1c) (with $r_0 = 1$ and $\Omega_0 = 1$) provides a simple model of the breaking-and-filamentation behavior of linearly unstable isolated vortices. We compare two runs without and with regularization, Table IIa (with $\mu = 0.0$) and Table IIb (with $\mu = 0.002$), respectively. The initial contour is a $1:\frac{1}{4}$ ellipse with $N(0) = 220$ nodes ($c_1 = 0.025$, $h_{min} = 0.01$, and $h_{max} = 0.025$). Table IIa shows a much more rapid growth in curvature than Table IIb. The former run terminated at $t = 4.60$ when the number of nodes demanded by the node-insertion algorithm

TABLE IIa

The Evolution of a 1: 0.25 Ellipse with Differential Rotation and $\Omega_0 = 1.0$, $r_0 = 1/2$, and $\mu = 0.0$.[a]

t	N	P	A_{tr}	ε_A	κ_{max}	κ_{min}
0.0	220	4.28920	0.78537	0	16.56	0.250
1.0	341	4.98618	0.78537	7.6	21.75	−154.0
2.0	412	6.50500	0.78537	14.1	45.57	−202.0
3.0	479	8.28297	0.78537	16.6	102.8	−201.0
4.0	582	10.16042	0.78537	16.6	214.0	−231.0

[a] Single precision, $\Delta t = 0.02$; $h_{min} = 0.01$ and $h_{max} = 0.025$.

TABLE IIb

The Evolution of a 1: 0.25 Ellipse with Differential Rotation and $\Omega = 1.0$, $r_0 = 1/2$, and $\mu = 0.002$[a]

t	N	P	A_{tr}	ε_A	κ_{max}	κ_{min}
0.0	220	4.28920	0.78537	0	16.56	0.250
1.0	294	4.80609	0.77279	−2.6	16.07	−23.08
5.0	636	9.60453	0.72254	−29.1	53.75	−13.01
6.0	716	10.61442	0.70997	−46.5	62.34	−12.34
7.0	791	11.49434	0.69741	−66.0	71.19	−11.88
8.0	887	12.32767	0.68484	−94.9	80.92	−11.57

[a] Single precision, $\Delta t = 0.02$; $h_{min} = 0.01$ and $h_{max} = 0.025$.

exceeded 900. The strange (increasing-decreasing) behavior of ε_A in Table IIa is due to the large-rapid fluctuations in curvature which develop in this unregularized run, as shown in Fig. 4c.

In Figs. 4a and 4b we present contour plots corresponding to the results in Tables IIa and IIb, respectively. In Figs. 4c and 4d we show curvature κ vs arc length corresponding to Figs. 4a and 4b. (Note, the ordinate varies geometrically.) The unregularized contour develops large values of $|\kappa|$, $O(10^2)$, that fluctuate rapidly over very short intervals near "corners." (For graphical convenience, curvature values are not plotted if $|\kappa| > 10^2$.)

The regularized contour shows a smooth growth in perimeter and a contraction in width of the filamentary arms. For convenience, we track three points in Figs. 4b and 4d with ●, *, $^+$. The ● is the location of the reference node for arc length, $s = 0$. (s increases counterclockwise.) Note at $t = 8$ the curvature at $s = 0$ is <0. The * is the location of the one tip, which persists and becomes the end of one of the filaments.

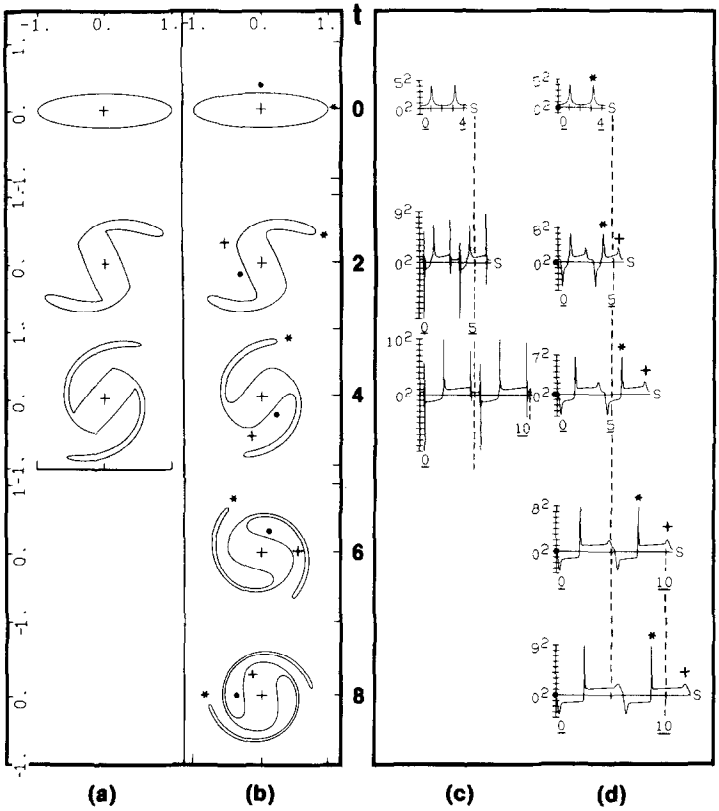

FIG. 4. Contour evolution of an initial 1: 0.25 ellipse with a prescribed differential rotation, (4.1c); (a) $\mu = 0$, Table IIa; (b) $\mu = 0.002$, Table IIb; (c) curvature vs arc length, $\mu = 0$, Table IIa; (d) curvature vs arc length, $\mu = 0.002$, Table IIb. The ●, *, and + in Figs. 4b and 4d show corresponding locations. (Note, the ordinate for curvature is a geometric scale: $\pm 1^2$, $\pm 2^2$, $\pm 3^3$,.... The arc length is zero at ● and increases in a counterclockwise direction.)

The magnitude of κ at * increases monotonically because the tip radius is decreasing. The maximum of κ at + results from the differential rotation and eventually decreases in time because of regularization. Note, that these extrema are properly resolved by the node-adjustment algorithm.

5. DISCUSSION

We have presented continuum equations for dispersive and dissipative tangential regularization of the motion of one contour. For the latter we have shown a correspondence for short times with the two-dimensional linear diffusion equation, $\omega_t = \nu \Delta \omega$. To obtain a more accurate correspondence at longer times will require a

multicontour model. The nature of the mutual interactions between contours is governed both by the advective $\hat{\mathbf{x}}_t$ and dissipative parts of the real evolutionary process. For example, Overman and Zabusky [22] have related the steepening of the "backside" of ion-density clouds to the overtaking and approach of contours. A proper *normal* direction regularization procedure will yield dynamical equations for the intercontour separation distance that results from a competition between an "approach" velocity due to $\hat{\mathbf{x}}_t$ and a "separation" velocity due to $\mu \nabla\omega$. This is analogous to the steep negative gradients that arise in solutions of the one-dimensional Burgers' equation (1.1) that result from a competition between uu_x and vu_{xx}.

APPENDIX A: CORRESPONDENCE OF TANGENTIAL REGULARIZATION AND 2D DIFFUSION

We shall now compare tangential regularization of a contour dynamical algorithm without convection

$$(x, y)_t = \mu(x_{ss}, y_{ss}), \qquad (x, y) \in \mathbb{R}^2, \tag{A.1}$$

to a two-dimensional dissipative motion

$$\omega_t = \nu \Delta\omega, \qquad (x, y) \in \mathbb{R}^2. \tag{A.2}$$

For (A.1) the initial contour Γ_0 is

$$\Gamma_0 = \{(x, y) \mid y = \varepsilon \cos mx\}, \qquad 0 < \varepsilon \ll 1, \quad \varepsilon^{1/2} m = O(1), \tag{A.3}$$

and the corresponding initial condition for (A.2) is $\omega(x, y, 0) \equiv \omega_0(x, y)$, where

$$\begin{aligned} \omega_0(x, y) &= 1 \qquad \text{for} \quad y < \Gamma_0, \\ &= 0 \qquad \text{for} \quad y > \Gamma_0. \end{aligned} \tag{A.4}$$

If we replace (x_{ss}, y_{ss}) in (A.1) by $\kappa(-\sin\phi, \cos\phi)$, then (A.1) becomes

$$(x, y)_t = \mu[(x_\sigma y_{\sigma\sigma} - y_\sigma x_{\sigma\sigma})/(x_\sigma^2 + y_\sigma^2)^2](-y_\sigma, x_\sigma), \tag{A.5}$$

where we have used (2.3) and (2.6) and σ parametrizes the contour.

We perform a perturbation analysis in the variables $\Sigma = m\sigma$ and $\tau = m^2 t$, where

$$\begin{aligned} x(\Sigma, \tau) &= \Sigma/m + \varepsilon x^{(1)} + \varepsilon^{3/2} x^{(2)} + \cdots, \\ y(\Sigma, \tau) &= \varepsilon y^{(1)} + \varepsilon^{3/2} y^{(2)} + \cdots, \end{aligned} \tag{A.6}$$

and

$$\begin{aligned} x^{(n)}(\Sigma, 0) &= 0 && \text{for} \quad n \geqslant 1, \\ y^{(n)}(\Sigma, 0) &= \cos mx && \text{for} \quad n = 1, \\ &= 0 && \text{for} \quad n \geqslant 2. \end{aligned} \tag{A.7}$$

The first- and second-order evolution operators are

$$\begin{aligned} x_\tau^{(1)} &= 0, & y_\tau^{(1)} &= \mu y_{\Sigma\Sigma}^{(1)}, \\ x^{(2)} &= -\mu m \varepsilon^{1/2} y_\Sigma^{(1)} y_{\Sigma\Sigma}^{(1)}, & y_\tau^{(2)} &= \mu y_{\Sigma\Sigma}^{(2)}, \end{aligned} \tag{A.8}$$

where we have made repeated use of $x_\sigma^{(1)} = 0$. Solving, we obtain

$$x = \sigma - \varepsilon^2 m \sin(2m\sigma)(1 - e^{-2\mu m^2 t})/4 + O(\varepsilon^2),$$

and

$$y = \varepsilon e^{-\mu m^2 t} \cos m\sigma + O(\varepsilon^2).$$

Omitting terms $O(\varepsilon^{3/2})$ or higher, we obtain

$$x = \sigma, \qquad y = \varepsilon e^{-\mu m^2 t} \cos mx. \tag{A.9}$$

The solution of (A.2) with (A.4) can be written as

$$\begin{aligned} \omega(x, y, t) &= (4\pi\nu t)^{-1} \int_{-\infty}^{+\infty} \int_{-\infty}^{+\infty} \omega(\xi, \eta, 0) \exp^{-[(x-\xi)^2 + (y-\eta)^2]/[4\nu t]} \, d\xi \, d\eta \\ &= (4\pi\nu t)^{-1} \int_{-\infty}^{+\infty} d\xi \, e^{-(x-\xi)^2/4\nu t} \int_{-\infty}^{+\varepsilon \cos m\xi} d\eta \, e^{-(y-\eta)^2/4\nu t}, \end{aligned}$$

or

$$\omega(x, y, t) = \tfrac{1}{2} + (4\pi\nu t)^{-1} \int_{-\infty}^{+\infty} d\xi \, e^{-(x-\xi)^2/4\nu t} \int_{y}^{\varepsilon \cos m\xi} d\eta \, e^{-(y-\eta)^2/4\nu t}. \tag{A.10}$$

We now seek a correspondence between the two solutions. Since the dissipation process in (A.2) instantaneously smooths ω_0 everywhere, a comparison is not unique. To compare the lowest-order contour dynamical solution (A.9), we choose a line $\tilde{y}(x, t)$ defined by $\omega(x, \tilde{y}, t) = \frac{1}{2}$, or

$$0 = \int_{-\infty}^{+\infty} d\xi \, e^{-(x-\xi)^2/4\nu t} \int_{\tilde{y}}^{+\varepsilon \cos m\xi} d\eta \, e^{-(\tilde{y}-\eta)^2/4\nu t}, \tag{A.11}$$

that is, a line at the original half-magnitude level. The second integral of (A.11) can be written as

$$\int_{\tilde{y}}^{+\varepsilon\cos m\xi} d\eta\, e^{-(\tilde{y}-\eta)^2/4\nu t} = (\pi\nu t)^{1/2}\,\mathrm{erf}(g)$$

$$= (4\nu t)^{1/2}(g - (g^3/3) + O(g^5)), \qquad \text{(A.12)}$$

where $g = (4\nu t)^{-1/2}(-\tilde{y} + \varepsilon\cos m\xi)$. We now assume that νt is sufficiently large so that

$$g^2 = (4\nu t)^{-1}(\tilde{y} - \varepsilon\cos mx)^2 \ll 1. \qquad \text{(A.13)}$$

The integral over the leading term in (A.11) yields

$$\tilde{y} = \varepsilon e^{-\nu m^2 t}\cos mx, \qquad \text{(A.14)}$$

which agrees with (A.9) if $\mu = \nu$. Thus, to first order the tangential regularization procedure agrees with two-dimensional dissipation. Note that the preceeding statement is derived under the assumptions that the comparison is made at $\omega = \frac{1}{2}$.

APPENDIX B: CONTOUR PARAMETERIZATION AND APPROXIMATION

In this apendix we describe how to obtain an analytical representation of the contour Γ passing through N nodes in the plane $\{x_j, y_j \mid 1 \leqslant j \leqslant N\}$. To parameterize the contour, we first calculate the straight-line distance between adjacent nodes $\Delta l_j = ((x_{j+1} - x_j)^2 + (y_{j+1} - y_j)^2)^{1/2}$. We use the set of points $\{l_j, x(l_j)\}$ and $\{l_j, y(l_j)\}$ to obtain the cubic spline representation $\tilde{\Gamma} = \{x(l), y(l) \mid 0 \leqslant l \leqslant P_l\}$, which passes through the original nodes. The tilde indicates that the parameterization is the *straight-line* segments and P_l is the corresponding perimeter.

Second, we calculate the arc length along $\tilde{\Gamma}$ between adjacent nodes, or

$$\Delta s_j = \int_{l=l_j}^{l=l_{j+1}} ((d\tilde{x}(l))^2 + (d\tilde{y}(l))^2)^{1/2}. \qquad \text{(B.1)}$$

This integral is evaluated using an *adaptive* quadrature routine based on Simpson's rule [23]. In all our numerical results the relative error is 10^{-5} and the absolute error 10^{-4}, although quite often the error in perimeter and area is much smaller.

Finally, with the arc length calculated by (B.1) we use the set of points $\{(s_j, x(s_j)\}$ and $\{s_j, y(s_j)\}$ to obtain two periodic cubic spline representations of the contour $\Gamma = \{(x(s), y(s) \mid 0 \leqslant s \leqslant P_s\}$. This is the parameterization used in all our calculations. For example, we can calculate the tangent angle ϕ and curvature κ for any s by

$$\tan\phi(s) = y'(s)/x'(s), \qquad \text{(B.2)}$$

and

$$\kappa(s) = x'(s)\,y''(s) - x''(s)\,y'(s), \qquad \text{(B.3)}$$

where

$$x'(s) = dx(s)/ds.$$

The area, $A = -\int_\Gamma y\,dx$, is calculated by discretizing the contour integral and again using the adaptive quadrature routine.

ACKNOWLEDGMENTS

This work was supported by the Office of Naval Research under contracts N00014-77-C-0520 and N00013-78-C-0074 (Task NR 062-583) and by the Naval Research Laboratory under contracts N00014-82-C-2003 and N00014-82-C-2030.

Note added in proof. With reference to the discussion following Eq. (1.3), J. Marsden has called our attention to the work of V. I. Yudovich ("Nonstationary flow of an ideal incompressible fluid," *Zh. Vychisl. Mat. i Mat. Fiz.* **3** (1963), 1032–1066) which shows that the two-dimensional Euler equations with initially piecewise-constant distributions of vorticity are a well-posed problem.

REFERENCES

1. M. S. LONGUET-HIGGINS AND E. D. COKELET, *Proc. Roy. Soc. Ser. A* **350** (1976), 1.
2. M. S. LONGUET-HIGGINS AND E. D. COKELET, *Proc. Roy. Soc. Ser. A* **364** (1978), 1.
3. G. R. BAKER, D. I. MEIRON, AND S. A. ORSZAG, *J. Fluid Mech.* **123** (1982), 477.
4. G. R. BAKER, D. I. MEIRON, AND S. A. ORSZAG, *Phys. Fluids* **23** (1980), 1485.
5. N. J. ZABUSKY, M. H. HUGHES, AND K. V. ROBERTS, *J. Comput. Phys.* **30** (1979), 96.
6. G. S. DEEM AND N. J. ZABUSKY, *Phys. Rev. Lett.* **40** (1978), 859. Also see the extended version, Stationary V-states, interactions, recurrence, and breaking, *in* "Solitons in Action" (K. Lonngren and A. Scott, eds.), pp. 277–294, Academic Press, New York, 1978.
7. E. A. OVERMAN II AND N. J. ZABUSKY, *Phys. Fluids* **25** (1982), 1297.
8. H. M. WU, E. A. OVERMAN II, AND N. J. ZABUSKY, New contour dynamical algorithm with adaptive node adjustment. A sensetivity approach for optimal algorithm selection, in preparation.
9. E. A. OVERMAN II AND N. J. ZABUSKY, *Phys. Rev. Lett.* **45** (1980), 1963.
10. E. A. OVERMAN II, N. J. ZABUSKY, AND S. L. OSSAKOW, *Phys. Fluids* **26** (1983), 1139.
11. H. M. WU, E. A. OVERMAN II, AND N. J. ZABUSKY, Steady-state solutions of the Euler equations in two dimensions: Rotating and translating V-states with limiting cases. I. Numerical algorithms and results, *J. Comput. Phys.* **53** (1984), to appear.
12. E. HOPF, *Comm. Pure Appl. Math.* **3** (1950), 201.
13. J. COLES, *Quart. Appl. Math.* **9** (1951), 232.
14. J. VON NEUMANN AND R. D. RICHTMYER, *J. Appl. Phys.* **21** (1950), 232.
15. R. D. RICHTMYER AND K. W. MORTON, "Difference Methods for Initial-Value Problems," 2nd ed., Interscience, New York, 1967. Equation (1.2) corresponds to Eq. (12.41) in Section 12.10. As explained in the footnote on p. 313, this equation is preferred to the one given in Ref. [14], namely, $q = \bar{\nu}\tau u_x |u_x|$.
16. R. F. WARMING AND R. M. BEAM, On the construction and application of implicit factored schemes for conservation laws, *in* "Computational Fluid Dynamics" (H. Keller, ed.), Vol. 11, pp. 85–129, SIAM–AMS Proceedings, Amer. Math. Soc., Providence, R. I., 1978.
17. H. A. ROSE AND P. L. SULEM, *J. Physique* **39** (1978), 441. Section 5 discusses "Rigorous Results for the Time-Dependent Euler Equations."

18. R. H. KRAICHNAN AND D. MONTGOMERY, *Rep. Prog. Phys.* **43** (1979), 547.
19. N. J. ZABUSKY AND G. S. DEEM, *J. Fluid Mech.* **47** (1971), 353.
20. K. A. BRAKKE, "The Motion of a Surface by Its Mean Curvature," Princeton Univ. Press, Princeton, N. J., 1978.
21. M. J. ABLOWITZ AND H. SEGUR, "Solitons and the Inverse Scattering Transform," SIAM Philadelphia, 1981.
22. E. A. OVERMAN II AND N. J. ZABUSKY, Contour dynamics: A boundary-integral evolutionary method for ionospheric plasma clouds, *in* "Proceedings of the 10th IMACS World Congress," Vol. I, pp. 205–207, 1982.
23. G. E. FORSYTHE, M. A. MALCOLM, AND C. B. MOLER, "Computer Methods for Mathematical Computations," Prentice-Hall, Englewood Cliffs, N. J., 1977.